

# Chapter 2

## Crystallographic Texture and Plastic Anisotropy

Hans Joachim Bunge and Robert Arthur Schwarzer

### 2.1 The Structure of Polycrystalline Materials

Anisotropy includes elastic and plastic anisotropy. The macroscopic anisotropy is closely related to the anisotropic behavior of the single crystal and to the structure of the polycrystalline material. The anisotropy of the elastoplastic behavior of the single crystal results from the crystallographic nature of plastic glide, interactions between the glide systems (reflecting the dislocation—dislocation—precipitation interactions) and eventually anisotropy of elastic constants. The mechanical anisotropy associated with the granular aspect of the material is caused by the crystallographic texture, morphology (size, shape and mutual arrangement of grains, grain boundaries) and internal stresses caused by intragranular incompatibilities of plastic strain. In cold rolled sheets, elastic deformation is much smaller than plastic deformation.

The structure of crystalline materials can be characterized by four structure levels:

1. The *Crystal Structure* specifies the kind and position of atoms in the unit cell of the ideal crystal lattice.
2. The *Phase Structure* specifies the sizes, shapes and mutual arrangement of single-phase volumes (volumes with constant crystal structure) in polyphase materials.
3. The *Grain Structure* specifies the sizes, shapes, crystal lattice orientations, and mutual arrangement of monocrystal volumes (within the single-phase volumes).

---

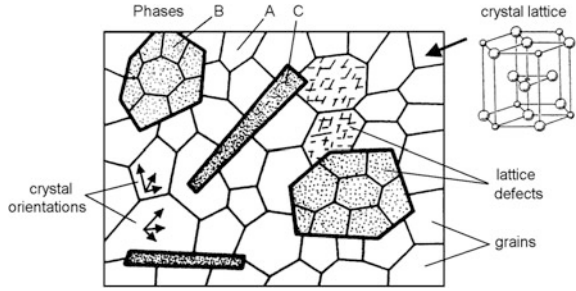
Hans Joachim Bunge—deceased.

---

R.A. Schwarzer (✉)  
Kappstr. 65, 71083 Herrenberg, Germany  
e-mail: [post@robert-schwarzer.de](mailto:post@robert-schwarzer.de)  
URL: <http://www.crystaltexture.com>

H.J. Bunge · R.A. Schwarzer  
Clausthal University of Technology, Leibnizstr. 4, 38678 Clausthal-Zellerfeld, Germany

**Fig. 2.1** The structure of a polycrystalline material can be characterized by four structure levels: crystal structure, phase structure, grain structure, substructure



4. The *Substructure* specifies the kind, amount, arrangement, crystallographic orientation of all lattice defects, i.e. all deviations from the ideal crystal lattice such as point defects, dislocations, stacking faults, grain and phase boundaries, the surface, elastic strain, magnetization, electric polarization.

This is illustrated schematically in Fig. 2.1. Any crystalline material is thus completely characterized by the *Microstructure Function*  $G(\mathbf{x})$  which specifies the phase, orientation and defects in all small (monocrystalline) volume elements  $V_x$  at the loci  $\mathbf{x}$  in the material (Bunge and Schwarzer 2001):

$$G(\mathbf{x}) = \left\{ \begin{array}{ll} i(\mathbf{x}) & \text{Phase Locus Function} \\ g(\mathbf{x}) & \text{Orientation Locus Function} \\ D(\mathbf{x}) & \text{Substructure Function} \end{array} \right\} \quad \text{Microstructure Function} \quad (2.1)$$

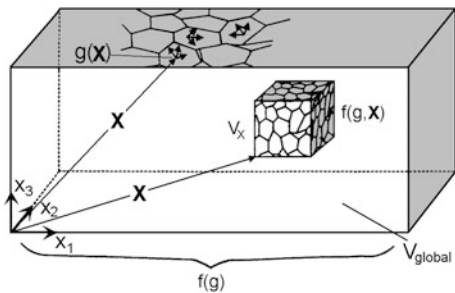
## 2.2 Definition of Crystallographic Texture

The term *Crystallographic Texture* or *Preferred Orientations*, in its widest sense, may be identified with the Orientation Locus Function  $g(\mathbf{x})$ . In a narrower (conventional) sense, however, it is understood as the set of volume fractions of all crystallites in the sample having any given crystal orientation  $g$ . Its mathematical formulation is the *Orientation Density Function* or *Orientation Distribution Function* ODF (Bunge 1982):

$$\frac{dV_g/V}{dg} = f(g); \quad g = \{\varphi_1, \Phi, \varphi_2\} \quad \text{Global Texture.} \quad (2.2)$$

The same definition can also be applied to smaller (but still polycrystalline) *subsamples* of the size  $V_x$  at the locus  $\mathbf{x}$  in the sample. The ODF in the subsample  $V_x$  is called the *Local Texture*, and all local textures together form a *Texture Field*. In order to make clear that the definition Eq. (2.2) applies to the *whole sample* it may then be called the *global texture*.

**Fig. 2.2** Illustration of the three texture functions: the global texture  $f(g)$ ; the local textures  $f(g, \mathbf{X})$  forming together a texture field; the orientation locus function  $g(\mathbf{x})$



$$\frac{dV_g/V_X}{dg} = f(g, \mathbf{X}); \quad \mathbf{X} = \{X_1, X_2, X_3\} \quad \text{Texture Field} \quad (2.3)$$

Finally, by considering still smaller (monocrystalline) subvolumes  $V_X$  at the locus  $\mathbf{X}$ , we obtain the complete *Orientation Locus Function*  $g(\mathbf{x})$  (contained in Eq. (2.1)) (Bunge and Schwarzer 2001)

$$g = g(\mathbf{x}); \quad \begin{aligned} g &= \{\varphi_1, \Phi, \varphi_2\} \\ \mathbf{x} &= \{x_1, x_2, x_3\}. \end{aligned} \quad \text{Orientation Locus Function} \quad (2.4)$$

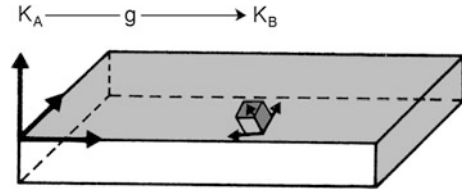
The Orientation Locus Function  $g(\mathbf{x})$  corresponds to a Cosserat continuum (Cosserat and Cosserat 1909) (if we do not take the atomistic structure of matter into account). The three definitions, Eqs. (2.2)–(2.4), are illustrated in Fig. 2.2. The ODF, Eq. (2.2), is three-dimensional, whereas texture fields and the Orientation Locus Function require six dimensions for their complete representation. Hence, if we want to “visualize” them, some further data reduction is required (to no more than three dimensions). In mathematical models of materials properties, e.g. the plastic properties as considered in this volume, both six-dimensional quantities, however, can be taken fully into account.

### 2.2.1 Crystal Orientation

The basic quantity in the Eqs. (2.2)–(2.4) is crystal orientation  $g$ . It is defined by choosing a crystallographic coordinate system  $K_B$  consisting of three crystal directions, e.g.  $[100][010][001]$  in cubic materials or  $[1\bar{1}00][11\bar{2}0][0001]$  in hexagonal materials. A second coordinate system,  $K_A$ , is (somehow) fixed in the sample. In sheet metals, for instance, one may choose the rolling, transverse and normal direction. In principle, the choice of both coordinate systems is deliberate.

It is, however, convenient to choose them in relation to symmetry, i.e. *sample symmetry* in the case of  $K_A$  and *crystal symmetry* in the case of  $K_B$ . An often considered sample symmetry is orthorhombic symmetry (which is in this case often

**Fig. 2.3** The orientation  $g$  of a single-crystalline volume element is described by the rotation which transfers the sample coordinate system  $K_A$  into the crystal coordinate system  $K_B$



called *orthotropic* symmetry). Crystal orientation  $g$  is the rotation which transfers  $K_A$  into  $K_B$ . This may be written in the form

$$K_B = g \cdot K_A \quad \text{Crystal Orientation} \quad (2.5)$$

and is illustrated in Fig. 2.3. Cubic-cubic coordinate systems are assumed. So a non-cubic crystal and/or a non-cubic sample coordinate system have to be defined first in orthonormal frames (Schumann 1979). Crystal orientation can be specified in many different “parameterizations”, e.g. by a transformation matrix  $[g_{ij}]$ , the Euler angles  $\{\varphi_1, \Phi, \varphi_2\}$ , a rotation axis  $\mathbf{r}$  and angle  $\omega$ , the Rodrigues vector, quaternions, or others:

$$g = [g_{ij}] = \{\varphi_1, \Phi, \varphi_2\} = \{\mathbf{r}, \omega\} \quad \text{Orientation Parameters.} \quad (2.6)$$

In this chapter we shall mainly use the Euler angles  $\{\varphi_1, \Phi, \varphi_2\}$  as was already done in Eqs. (2.2) and (2.4).

### 2.3 Experimental Determination of Textures

Texture measurement in the classical sense, Eq. (2.2), can be carried out with a *Texture Goniometer*, Fig. 2.4, using X-ray or Neutron Diffraction. The “output” of such an instrument are *Direction Distribution Functions*,  $P_{(hkl)}(\alpha, \beta)$ , of the normal directions  $\mathbf{h}$  to low-index reflecting crystal lattice planes (hkl) which are commonly called *Pole Figures* (Wassermann and Grewen 1962):

$$\frac{dV/V}{d\Omega} = P_{(hkl)}(\alpha, \beta) = \frac{1}{2\pi} \int_{\mathbf{h} \parallel \{\alpha\beta\}} f(g) dg; \quad d\Omega = \sin \alpha d\alpha d\beta \quad \text{Pole Figure} \quad (2.7)$$

where  $(\alpha, \beta)$  specifies a direction referred to the sample coordinate system  $K_A$ . These functions are two-dimensional projections of the three-dimensional function  $f(g)$  as is expressed on the right hand side of Eq. (2.7). The function  $f(g)$  can be calculated from several pole figures by a mathematical procedure, solving the

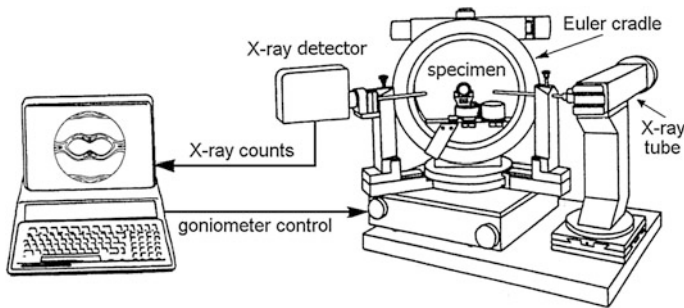


**Fig. 2.4** An automated X-ray texture goniometer (schematic) consisting of a two-circle diffractometer supplemented by a Eulerian Cradle as the sample orientation device

integral equation (Eq. (2.7)), called *Pole Figure Inversion* as shown schematically in Fig. 2.5. “Experimental” pole figures measured in reflection mode of X-ray diffraction are incomplete with a non-acquired circular range at large angles of specimen tilt. Since the ODF represents the full orientation distribution of the sampled volume, complete “theoretical” pole figures, however, can be recalculated from the ODF. For more details see e.g. Bunge (1982); Spiess et al. (2016).

In order to measure local textures and texture fields, a collimated fine primary beam (X-rays or synchrotron radiation), e.g. of 0.05 mm in diameter, is used and the specimen is scanned in steps of similar size. This can be done with an *X-ray Scanning Apparatus* which is essentially an “upgraded” conventional texture goniometer with a computer-controlled x-y specimen stage (see e.g. (Fischer and Schwarzer 1998; Schwarzer 2005)). Pole intensity distribution maps (Fig. 2.6a), texture fields,  $f(g, \mathbf{X})$ , and pole figures of small selected specimen areas are acquired. In addition residual lattice strain is determined simultaneously with the same high spatial resolution by evaluating the profile and shift of the X-ray diffraction peaks (Fig. 2.6b). If “white” primary X-rays and an energy dispersive X-ray detector are employed, the chemical composition can furthermore be obtained by X-ray micro-fluorescence analysis (XFA), and thus—in combination with checking for characteristic diffraction peaks—the Phase Locus Function  $i(\mathbf{x})$  is so acquired (Schwarzer 2005).

The complete Microstructure Function  $G(\mathbf{x})$  (at least in a two-dimensional section  $\mathbf{x} = \{x_1, x_2, 0\}$ ), Eq. (2.1), can be measured by backscatter electron diffraction in the *Scanning Electron Microscope* as is shown schematically in Fig. 2.7 (see e.g. (Schwarzer 1997; Schwartz et al. 2009)). The results of such measurements, known as EBSD (*Electron Backscatter Diffraction*) or COM (*Crystal Orientation Microscopy*), may be visualized by color-coding of  $g(\mathbf{x})$  in microstructural images as is shown, as an example, in Fig. 2.8. For the use in mathematical models e.g. of plastic anisotropy, the individual grain orientations of the Orientation Locus Function  $g(\mathbf{x})$  are available in the complete six-dimensional form, Eq. (2.4) (or at least five-dimensional if measurement is restricted to one sample plane). Phases can be discriminated simultaneously to determine the Phase

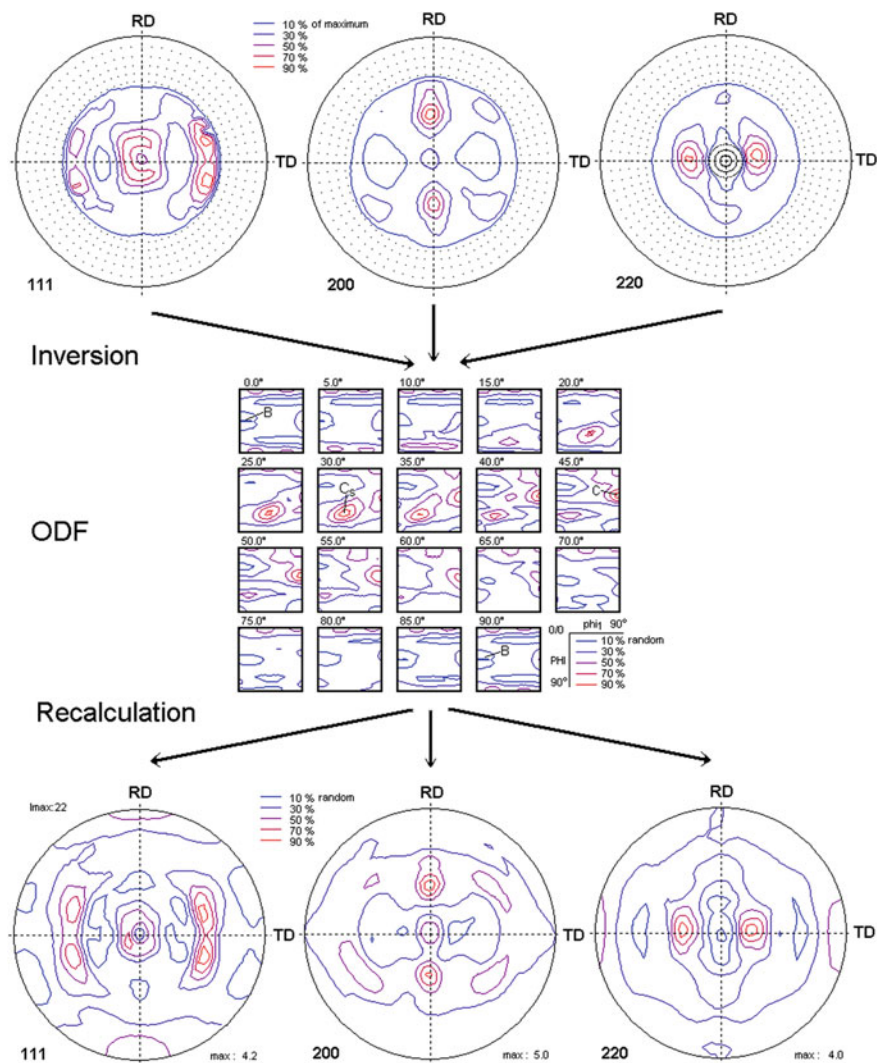


**Fig. 2.5** Calculation of the Orientation Distribution Function (ODF) (*center*) from several incomplete experimental pole distribution functions (*top*). The procedure is called “Pole Figure Inversion”. From the ODF complete pole figures can be recalculated (*bottom*)

Locus Function  $i(\mathbf{x})$  by checking, in a trial with all assumed crystal structures, for best indexing the diffraction patterns if the lattice constants differ sufficiently, as well as by supplementing electron beam microanalysis (Energy Dispersive X-Ray Spectroscopy, EDS, or Auger Electron Spectroscopy, AES). The pattern quality (PQ), i.e. the sharpness of the backscatter Kikuchi patterns, is a (semi-)quantitative measure of the perfection of the diffracting crystallite volume thus providing an estimate of the Substructure Function  $D(\mathbf{x})$ .

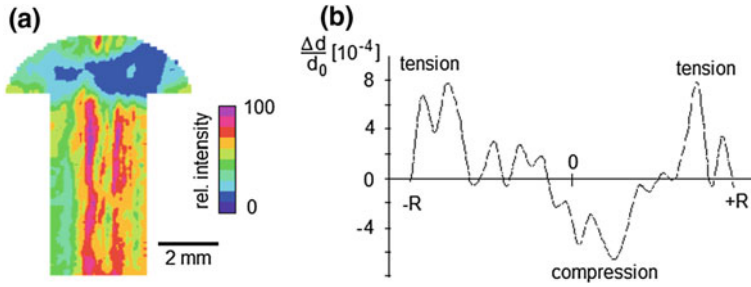


**Fig. 2.6** Cross section of an aluminum rivet. **a** Spatial distribution map of the 220 pole intensity. The 220 planes were placed parallel to the reference direction  $\alpha = 35^\circ$  and  $\beta = 83^\circ$ ,  $2\theta = 40.2^\circ$ ; **b** The lattice strain across the rivet bolt was calculated from the width of the 220 peaks

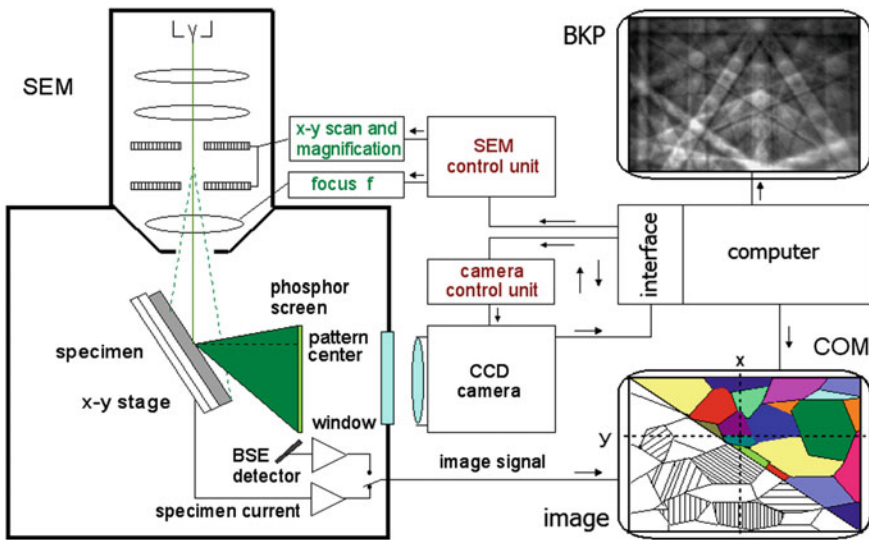


**Fig. 2.7** Backscatter electron diffraction in a scanning electron microscope (schematic). The points  $(x, y)$  on the specimen are scanned automatically. A wide-angle Kikuchi diffraction pattern (see insert on *top right*) is acquired in every point with a sensitive CCD camera, evaluated automatically for crystal orientation, and represented by a pixel with orientation specific color on the monitor screen to form a crystal orientation map (COM) (Schwarzer 1997)

The properties of a polycrystalline aggregate depend markedly on the arrangement and distribution of its constituent elements of all four structure levels as stated in Sect. 2.1. Hence, the general concept of orientation stereology, rather than merely texture or conventional stereology alone (i.e. Quantitative Materialography), must be taken as a basis for comprehensive models which describe and simulate anisotropic properties of the real polycrystalline material. Orientation stereology is based on the Microstructure Function  $G(\mathbf{x})$ , Eq. (2.1). Both fields of materials science, texture and



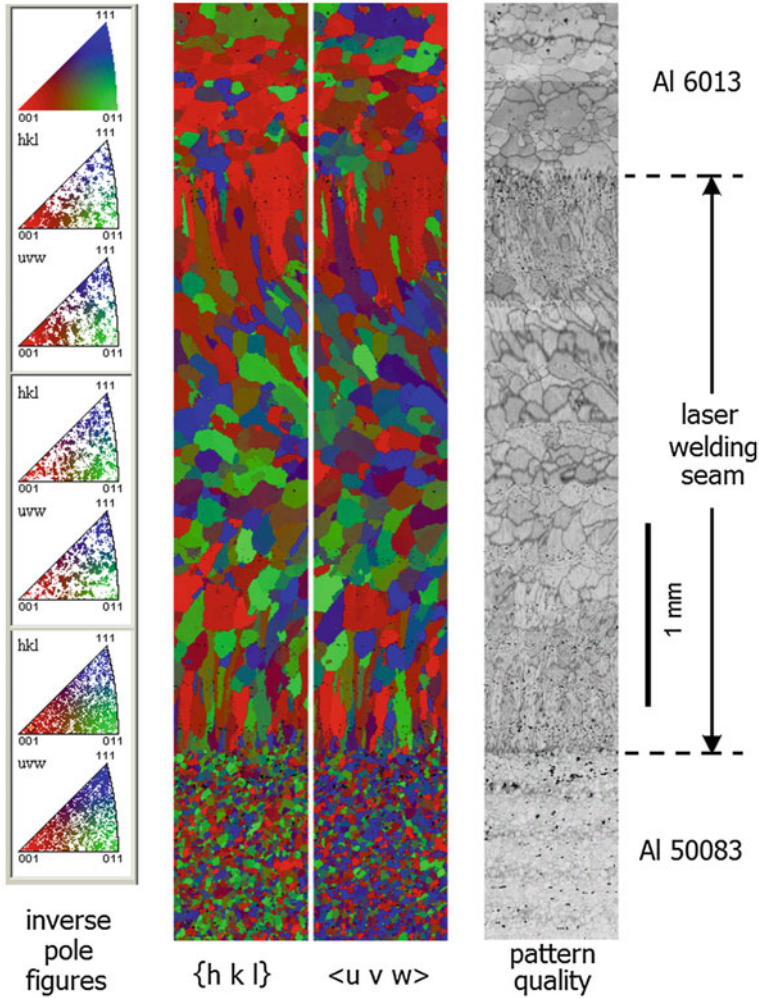


**Fig. 2.8** Representation of individual crystal data  $g(\mathbf{x})$  by *color coding*. A laser welding seam connects an Al6013 with an Al5083 metal sheet. The crystal directions,  $\{hkl\}$  in welding direction and  $\langle uvw \rangle$  in the reference direction (perpendicular to the welding direction and in the sheet plane), have been coded by the color triangle (*top left*) to form crystal orientation maps. The inverse pole figures of Al6013 (*upper left*), of the welding seam (*center left*), respectively of Al5083 (*bottom left*) have been constructed from the individual grain orientations. The grain structure is clearly reproduced in the pattern quality map (PQ) (Brokmeier et al. 2007)

stereology, and their conventional functions characterizing the microstructure are contained, but many other functions can be derived from  $G(\mathbf{x})$  which are hard or in no way accessible to direct measurement (Bunge and Schwarzer 2001).



## 2.4 Texture and Properties of Materials

Crystallographic texture, or even more generally the Microstructure Function  $G(\mathbf{x})$ , influences the physical properties of materials as is shown schematically in the right half of Fig. 2.9. On the other hand, texture is formed (or modified) by physical processes as is shown schematically on the left side of Fig. 2.9. With respect to the topic of this book we consider here particularly *Plastic Anisotropy* as a property and *Plastic Deformation* as a process. In technological forming processes both are directly related to each other as is also illustrated in this figure. The relationships are to be expressed in terms of mathematical models. It is evident that the relationship Process  $\rightarrow$  Structure  $\rightarrow$  Properties, illustrated in Fig. 2.9, holds for virtually all crystalline materials, be they metals, ceramics, (partly) crystalline polymers, or even geologic or natural biologic materials.

Crystallographic texture influences the properties of a material via *Crystal Anisotropy* as is illustrated schematically in Fig. 2.10:

- If the orientation distribution of the crystallites is not random, then the material may be macroscopically anisotropic. The effect can be understood (at least in a good first approximation) in terms of the classical texture function  $f(g)$ . This is the main topic of this chapter.
- At the grain boundaries the (local) properties are discontinuous. This may have a strong influence on the material's properties, too, even if the material is macroscopically isotropic.
- And finally the near-boundary zones of the crystallites may have deviating physical properties (e.g. higher diffusion or lower strength).

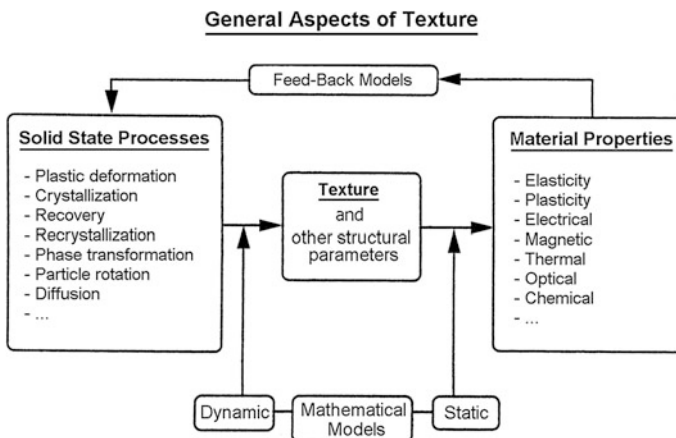


**Fig. 2.9** The two aspects of texture analysis: the “Process  $\rightarrow$  Texture” relationship (*left side*); the “Texture  $\rightarrow$  Property” relationship (*right side*)

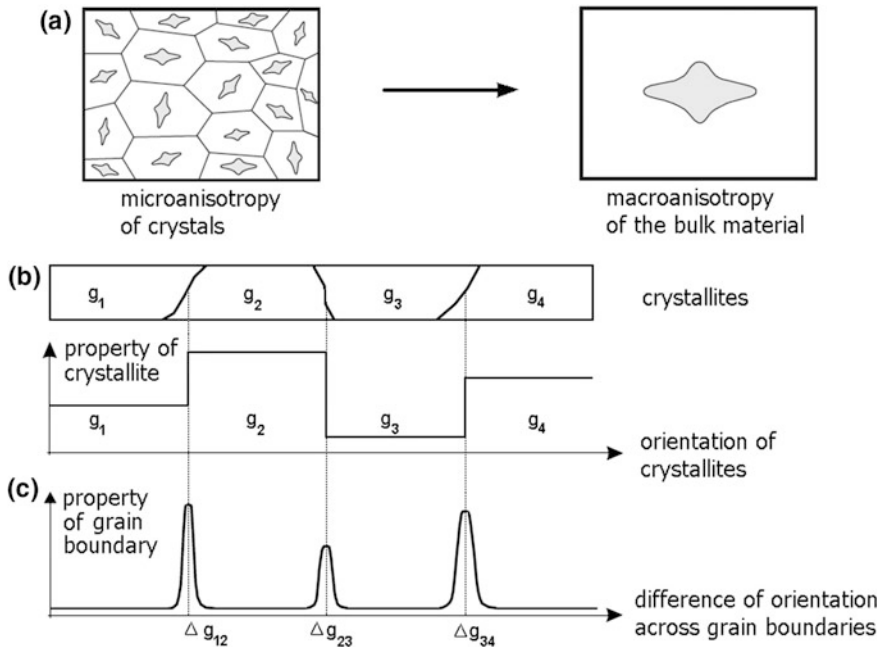
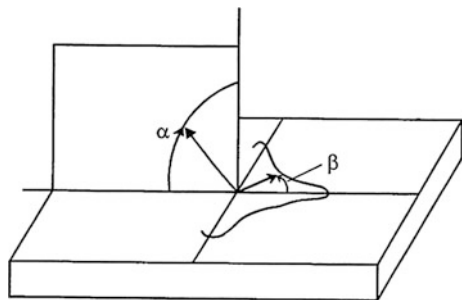


**Fig. 2.10** Effect of crystal anisotropy on material properties (schematic): **a** macro-anisotropy, **b** micro-discontinuity, **c** grain boundary properties

These latter two effects require the full Orientation Locus Function  $g(\mathbf{x})$  for their understanding rather than only the classical concept of texture  $f(g)$ .

In this book plastic formability of materials is considered for sheet materials. In this case it is convenient to subdivide plastic anisotropy into planar and normal anisotropy, as is shown schematically in Fig. 2.11. The *normal anisotropy* influences the maximum drawability of sheet material and should thus be as high as possible, as is shown in Fig. 2.12. For the correlation of  $r$  with deep-drawability see also Chap. 5.

**Fig. 2.11** The anisotropy of sheet material is subdivided into normal and planar anisotropy



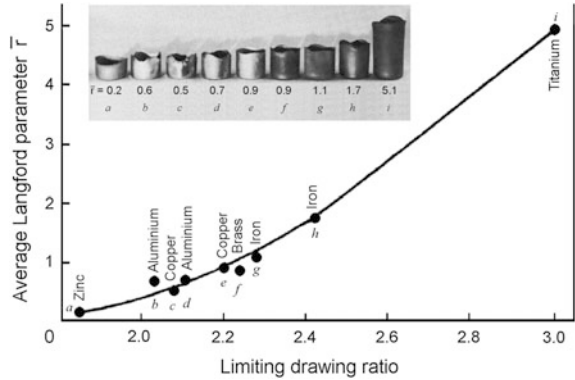


**Fig. 2.12** Normal anisotropy expressed by the average  $r$ -value enhances the deep drawability of sheet metals. The same material, e.g. aluminum, copper, iron, may have different textures and hence different  $\bar{r}$ -values (after (Wilson 1966))

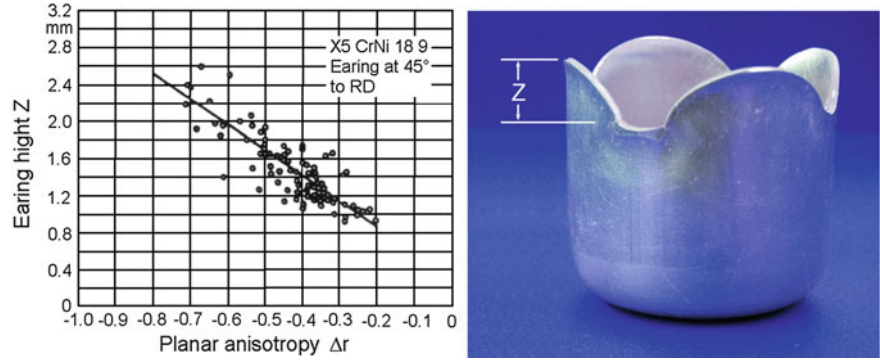


**Fig. 2.13** Planar anisotropy expressed by  $\Delta r$  leads to earing after deep drawing

*Planar anisotropy* leads to earing as is shown in Fig. 2.13. Hence, it should be as low as possible, ideally it should be zero. Both quantities are directly related to crystallographic texture. In fact, earing shown in Fig. 2.13 and the means how to avoid it, has become the very mark of crystallographic texture (see e.g. (Wassermann and Grewen 1962)).

## 2.5 Plasticity of Polycrystalline Materials

Plasticity of crystalline materials must be considered on many different length-scales as is illustrated in Fig. 2.14. The following scales may be distinguished:

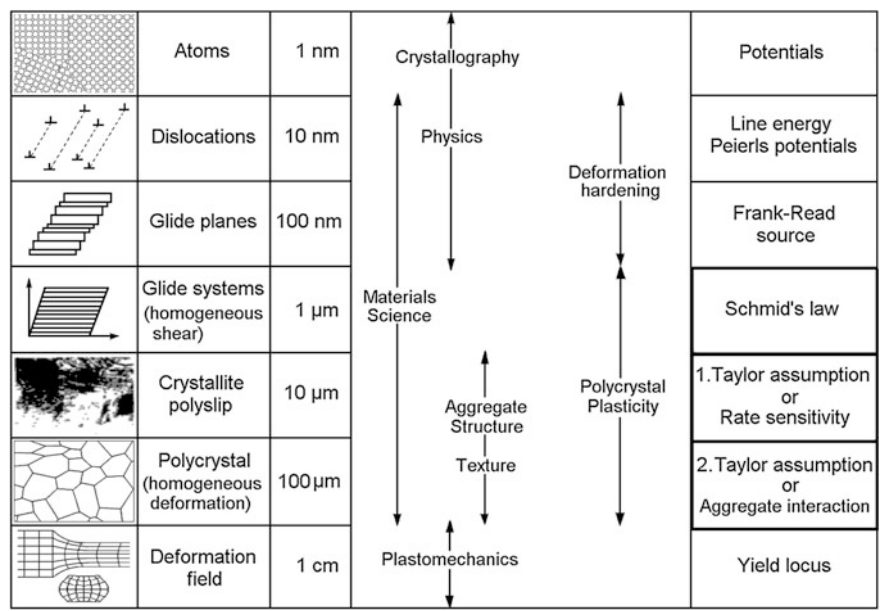


**Fig. 2.14** Plasticity of polycrystalline materials is to be considered on many different length scales ranging from atomistic to macroscopic-technological dimensions

Microscopic	→	Hardening relevant
Mesoscopic	→	Texture relevant
Macroscopic	→	Process relevant.

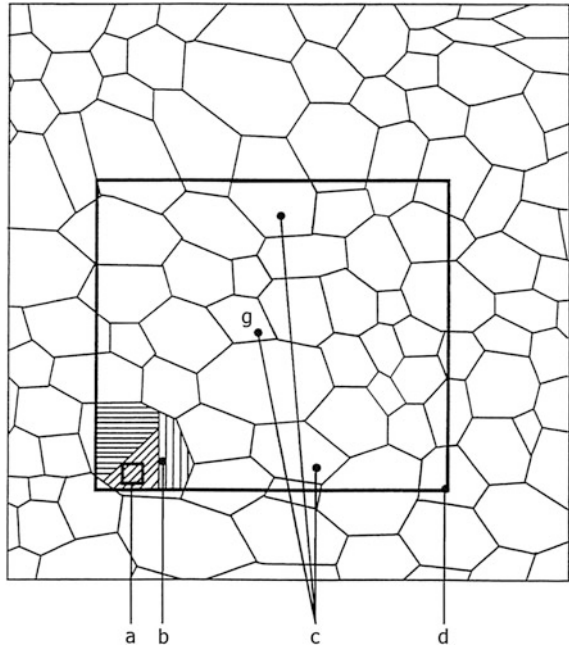
In this chapter we consider mainly the mesoscopic—texture relevant—scale. As is illustrated in Fig. 2.15, two volume elements of different length scales are distinguished:

- A small *monocrystalline* volume element (a) at the locus  $\mathbf{x}$ , with the crystal orientation  $g$ , Eq. (2.4), which undergoes *homogeneous* deformation  $\varepsilon(\mathbf{x})$  (as the average of individual dislocation movements considered on the microscopic scale).
- A bigger, *polycrystalline* volume element (d) at the locus  $\mathbf{X}$  with the texture  $f(g)$ , Eq. (2.3), which undergoes the *quasi-homogeneous* deformation  $\bar{\varepsilon}(\mathbf{X})$  (as the average of the local deformations  $\varepsilon(\mathbf{x})$  of all monocrystalline volume elements (a) which it contains).

Any mathematical model of polycrystal plasticity must contain *model assumptions* about the monocrystalline as well as the polycrystalline volume element. Plastic deformation of the *monocrystalline* volume element has been considered in terms of the following models:

- The *Sachs model* assumes glide in only *one glide system* which is subjected to the highest shear stress according to its maximum Schmid factor (Sachs 1928).

**Fig. 2.15** Different volume elements considered in a polycrystalline material: *a* small volume element which is single crystalline with homogeneous deformation,  $V_x$ , *b* single crystalline with inhomogeneous deformation, *c* volume fraction with same orientation *g*, *d* bigger polycrystalline volume  $V_x$  with texture  $f(g)$



- The *viscoplastic (strain rate sensitive) model* assumes glide in *all glide systems*. The glide rates  $\gamma^n$  in these systems depend on the shear stresses  $\tau^n$  falling into the systems (according to their Schmid factors).

$$\gamma^n = \gamma_0 \cdot \left[ \frac{\tau^n}{\tau_0^n} \right]^{\frac{1}{m}} \quad (2.8)$$

The exponent  $m$  is a measure of strain rate sensitivity (Canova et al. 1984; Tóth et al. 1997).

- The *Taylor-Bishop-Hill model* assumes glide in *all glide systems*. The glide rates  $\gamma^n$  guarantee minimum deformation work (see Eq. (2.13)) (Bishop and Hill 1951; Taylor 1938).

Also the *polycrystalline* volume element has been considered with different model assumptions:

- The *Taylor-Bishop-Hill model (full constraints)* assumes constant deformation throughout the whole material

$$\varepsilon(\mathbf{x}) = \bar{\varepsilon}(\mathbf{X}). \quad (2.9)$$

This assumption allows the polycrystalline volume element to be treated solely on the basis of the classical texture  $f(g)$ , Eq. (2.3).

- The *relaxed constraints (Taylor) model* allows deviations from Eq. (2.9). Particularly one or two shear strain components in  $\varepsilon(\mathbf{x})$  are “relaxed”, i.e. they are allowed to assume non-fixed values which are deduced, later on, from the model (Honneff and Mecking 1978).
- The *self-consistent model* considers one grain with the orientation  $g$  (at a time) individually which is embedded in a homogeneous matrix the properties of which are texture averages over all orientations  $g$  according to the texture  $f(g)$  (Kröner 1961; Molinari et al. 1987; Tomé and Canova 1998).
- Finally, model calculations have also been carried out *without any model hypotheses about the polycrystal*, i.e. they are based on the Orientation Locus Function  $g(\mathbf{x})$ , Eq. (2.4), the changes of which follow as a result of the model (Dawson et al. 1994; Dawson and Beaudoin 1998).

All of the polycrystal assumptions may be combined with any of the monocrystal assumptions, hence leading to a great variety of different model variants.

Plastic deformation is necessarily combined with *elastic deformation*. Hence, strictly speaking plasticity cannot be considered without taking elasticity into account. The maximum elastic strains are, however, much smaller than the maximum plastic strains. This applies particularly to metal forming processes in which the elastic strains can be neglected as compared with the plastic ones. It does not apply to the range of yield stresses, i.e. to the very onset of plasticity.

In this case some of the crystallites may have already been deformed plastically, whereas others are still in the elastic range. Hence, all models of plastic anisotropy and plastic deformation have been considered in two approximations, i.e. with and without elasticity (see e.g. (Iwakuma 1984; Masson and Zaoui 1999)).

Reviews over the various models are given, for instance, in (Van Houtte 1984, 1996; Kocks et al. 1998; Leffers et al. 1988; Leffers 1988; Lowe et al. 1991; Raabe 1998; Zaoui 1986). In the following we shall consider the full-constraints Taylor model in some more detail.

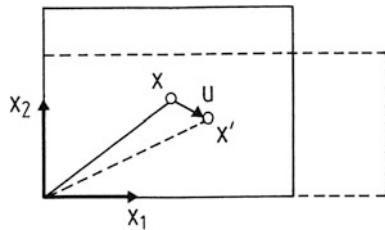
### 2.5.1 The Taylor Model (Full-Constraints)

Plastic deformation in a small volume element,  $V_{\mathbf{x}}$ , may be described by the displacement vector  $d\mathbf{u}$  of a point  $\mathbf{x}$  after a small deformation step  $d\eta$

$$du_i = d\eta \cdot \varepsilon_{ij} \cdot x_j \quad (2.10)$$

as is illustrated schematically in Fig. 2.16.

**Fig. 2.16** A small deformation step  $d\eta$  in a small volume element characterized by the displacement vector  $\mathbf{u}$



### Monocrystalline Volume Element

If the volume element is *monocrystalline* the deformation tensor  $\varepsilon_{ij}$  is composed of glide deformations in the glide systems  $n$  with the glide rates  $\gamma^n$ . Glide in one glide system is assumed to be a homogeneous shear described by the shear tensor (averaged over individual dislocation glide)

$$G_{ij}^n(g) = \mathbf{d}_i^n \cdot \mathbf{n}_j^n \quad (2.11)$$

with  $\mathbf{d}$  being the vector of the glide direction and  $\mathbf{n}$  the normal to the glide plane, respectively (referred to the chosen *sample* coordinate system  $K_A$ ).

In a given crystal structure, glide plane and glide direction are usually known with respect to the *crystal* coordinate system  $K_B$ , e.g. in the form  $\{hkl\}\langle uvw \rangle$  as glide plane and glide direction. In fcc metals, for instance, the glide systems  $\{111\}\langle 110 \rangle$  are assumed active. The orientations of the glide systems must be transformed by the rotation  $g$ , using the transformation matrix  $[g_{ij}]$ , Eq. (2.6), into the sample coordinate system  $K_A$  which was assumed in Eq. (2.11).

Plastic deformation may also proceed by twinning which we do not consider here for the sake of simplicity. Diffusion processes such as grain boundary glide are not taken into account here either.

Glide, by itself, does not change the orientation of the crystal lattice. However, the external forces may induce a torque on the deformed volume element which leads to a rigid rotation  $R$  as is illustrated schematically in Fig. 2.17. Hence, the

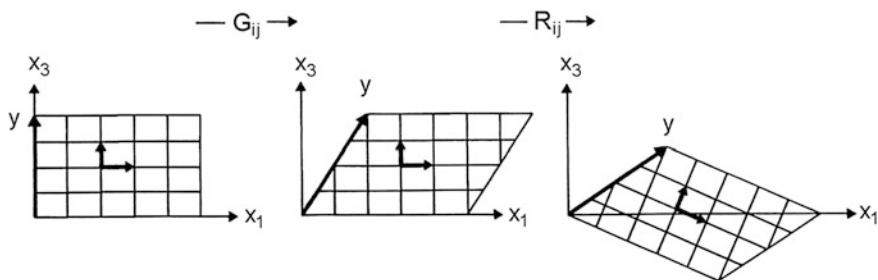


**Fig. 2.17** Plastic deformation of a single-crystalline volume element by glide and rigid rotation. The intermediate state (only glide without rotation) is only imaginary



deformation tensor  $\varepsilon_{ij}$  in Eq. (2.10) must be composed of glide in all glide systems and a rigid rotation  $R$ :

$$\varepsilon_{ij} = \sum_{n=1}^N \gamma^n \cdot G_{ij}^n(g) + R_{ij}. \quad (2.12)$$

In most cases, the number  $N$  of available glide systems is greater than the number of independent components in  $\varepsilon$ . Hence, Eq. (2.12) leaves a high degree of freedom to the choice of the  $\gamma^n$ . Any physically realistic choice must, however, guarantee minimum deformation work which requires

$$\sum_{n=1}^N |\gamma^n| a^n = \min \rightarrow M; \quad a^n = \tau_0^n / \tau_0 \quad (2.13)$$

where  $\tau_0^n$  are the critical resolved shear stresses in the glide systems, and  $\tau_0$  is some average value of them. In Eqs. (2.12) and (2.13),  $\varepsilon_{ij}$  and  $g$  are the *input variables*, the rotation  $R_{ij}$  and the Taylor factor  $M$  are the *output quantities* of the model, the glide system tensors  $G_{ij}^n$  described by  $\mathbf{d}$  and  $\mathbf{n}$ , Eq. (2.11), depend on the crystal structure of the considered material, and the critical resolved shear stresses  $\tau_0^n$  depend on the state of deformation hardening reached after a finite degree  $\eta$  of deformation, i.e. they depend on  $D(\mathbf{x})$ , Eq. (2.1).

The matrices  $\varepsilon_{ij}$ ,  $G_{ij}$ ,  $R_{ij}$  in Eq. (2.12) may be split into their respective symmetric and antisymmetric parts. Hence, Eq. (2.12) can be written in the form

$$\varepsilon_{ij}^{\text{sym}} = \sum_{n=1}^N \gamma^n \cdot G_{ij}^n(g)^{\text{sym}} \quad (2.12a)$$

$$\varepsilon_{ij}^{\text{ant}} = \sum_{n=1}^N \gamma^n \cdot G_{ij}^n(g)^{\text{ant}} + R_{ij}. \quad (2.12b)$$

Since  $R_{ij}$  is antisymmetric it is not contained in Eq. (2.12a). Hence, this equation can be solved together with Eq. (2.13) for the  $\gamma^n$ . In the most general case this system of equations has several linearly independent solutions  $\gamma_m^n$  (notwithstanding the minimum condition in Eq. (2.13) which enforces a *unique* solution for  $M$ ). Substituting the  $\gamma_m^n$  in Eq. (2.12b) gives the rotations  $R_{ij}^m$  which are thus also not unique. Hence, the Taylor model has two (external) output quantities

$$M(\varepsilon_{ij}, g) \quad \text{Taylor Factor} \quad (2.14)$$

$$R_{ij}(\varepsilon_{ij}, g) = \sum_m \alpha^m \cdot R_{ij}^m(\varepsilon_{ij}, g) \quad \text{Axis Rotation Rate.} \quad (2.15)$$

(Then the “internal” quantities  $\gamma_m^n$  are no more required.) The Taylor factor  $M$  expresses the deformation work  $dW$  needed during the deformation step  $d\eta$ , Eq. (2.10). It is

$$dW = d\eta \cdot \tau_0 \cdot M. \quad (2.16)$$

Hence, its dependence on  $\varepsilon_{ij}$ , Eq. (2.14) describes the plastic anisotropy of the monocrystalline volume element.  $M$  has been called the *plastic potential*. It is the basis for the calculation of the plastic properties of the material (for small deformations).

The rigid rotation rate  $R$  changes the crystallographic orientation  $g$  of the volume element by  $\Delta g$

$$\Delta g = d\eta \cdot R \quad \text{Lattice Spin.} \quad (2.17)$$

Corresponding to the Cosserat continuum (Lippmann 1969, 1995) this may be called the “lattice spin” of the monocrystalline volume element. The Cosserat theory of elasticity, also known as micropolar elasticity, incorporates the translation due to force stress assumed in classical elasticity as well as a local orientation of volume elements due to a couple stress (torque). Lattice spin is the basis for the change of texture in the course of plastic deformation. Considered as a function of the starting orientation  $g$  it describes the *Orientation Flow Field* (in the orientation space) (Bunge and Klein 1993, 1991).

The Taylor model does not fix the factors  $\alpha^m$  in Eq. (2.15) which may assume any values under the conditions

$$\sum_m \alpha^m = 1; \quad 0 \leq \alpha^m \leq 1. \quad (2.18)$$

The actual values of the  $\alpha^m$  depend on the environment of the considered volume element, i.e. on  $g(\mathbf{x})$  in this environment. They may also be influenced by the local defect substructure  $D(\mathbf{x})$ , Eq. (2.1). These quantities are, however, not taken into consideration in the classical Taylor model. Rather, as was mentioned in the context of Eq. (2.9), this model stays within the scope of the classical texture function  $f(g)$ . Hence, within the Taylor model, some reasonable assumptions for some average values of the  $\alpha^m$  are usually introduced (see e.g. (Chin 1969)). It is worth mentioning that the non-uniqueness of the rotation  $\Delta g$ , for volume elements with the same starting orientation  $g$ , leads to deformation textures which are flatter than the ones described later on in Eq. (2.24). For details see e.g. (Bunge and Klein 1993).

In Fig. 2.18 the Taylor factor is shown as a function of crystal orientation  $g$ , calculated for plane-strain deformation  $q = 0$  (see Eq. (2.26)) for fcc metals with the glide systems  $\{111\}\langle 110 \rangle$  (Bunge 1970). In Fig. 2.19 one section,  $\varphi_1 = 90^\circ$ , of the orientation flow field is shown for the same parameters as for the Taylor factor in Fig. 2.18 (Bunge 1970).

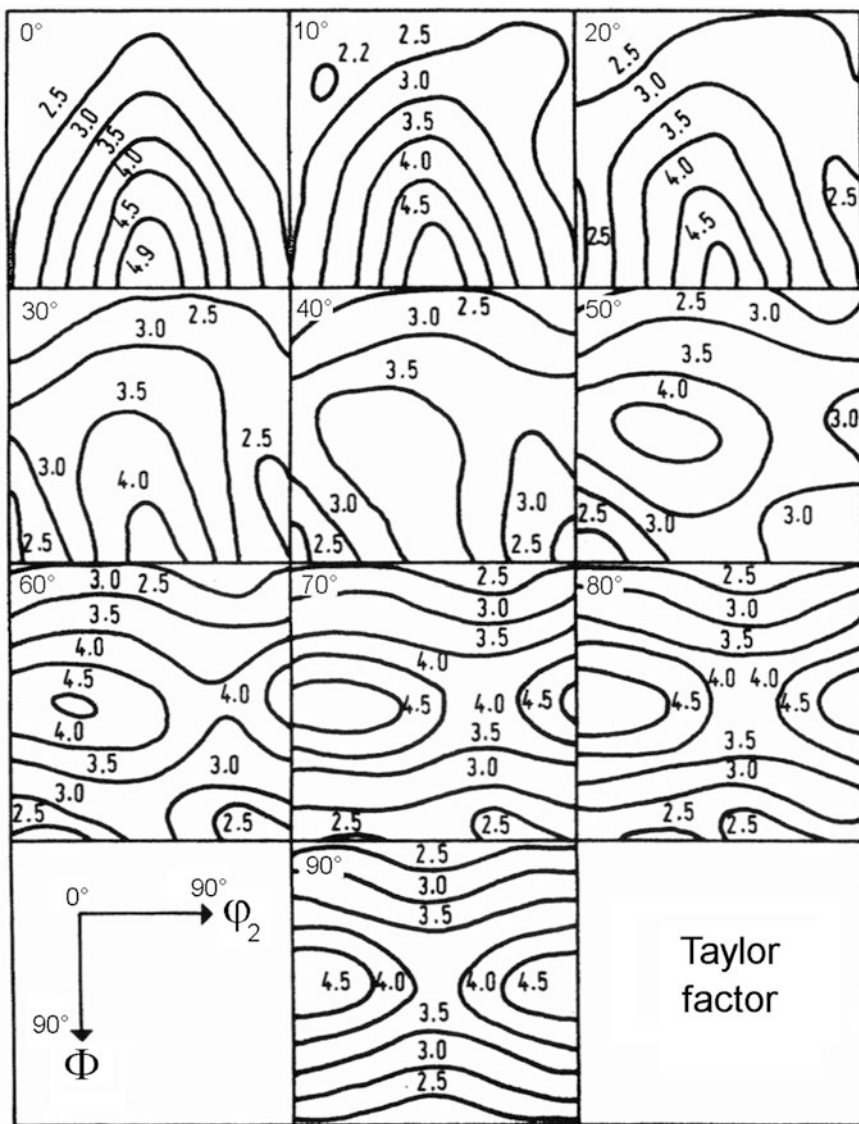
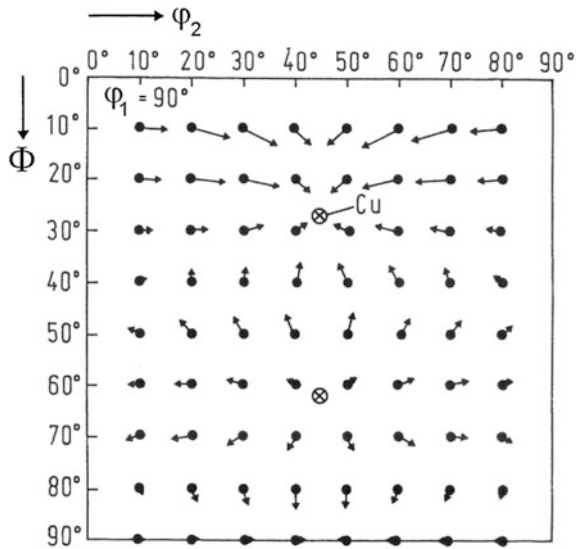


**Fig. 2.18** The single-crystal Taylor factor  $M(g)$  as a  $g$  function of crystal orientation expressed by Euler angles  $\varphi_1$ ,  $\Phi$ ,  $\varphi_2$

### Polycrystalline Volume Element

The monocrystal quantities  $M$  and  $R$ , Eqs. (2.14) and (2.15), are to be averaged in the *polycrystalline volume element*  $V_X$  with the texture  $f(g)$  as weight function:

**Fig. 2.19** Lattice rotation  $R(g)$  as a function of the initial orientation  $g$  (only one section,  $\phi_1 = 90^\circ$ , of the Euler space is shown). Crystal orientations rotate toward the main orientation (Cu) of the copper rolling texture



$$\overline{M}(\epsilon_{ij}) = \int_g M(\epsilon_{ij}, g) \cdot f(g) dg \quad (2.19)$$

$$\overline{R}_{ij}(\epsilon_{ij}) = \int_g R_{ij}(\epsilon_{ij}, g) \cdot f(g) dg. \quad (2.20)$$

The polycrystal Taylor factor  $\overline{M}$  expresses the deformation work needed during the deformation step  $d\eta$  in the polycrystalline volume element  $V_X$

$$d\overline{W} = d\eta \cdot \tau_0 \cdot \overline{M}. \quad (2.21)$$

Hence, its dependence on  $\epsilon_{ij}$ , Eq. (2.19) describes the plastic anisotropy of this volume element. It is the *plastic potential* for this volume element.

The averaged rotation rate  $\overline{R}$  describes a “common” rotation component of all monocrystalline volume elements contained in the polycrystalline one, Fig. 2.20. If the crystallites would do only this rotation, the texture  $f(g)$  would only be rotated *as a whole* to the new one

$$f'(g) = f(\overline{\Delta}g \cdot g); \quad \overline{\Delta}g = d\eta \cdot \overline{R} \quad \text{Texture Spin.} \quad (2.22)$$

With reference to the Cosserat continuum (Lippmann 1969, 1995) this may be called the *Texture Spin*. It is, however, evident from Fig. 2.20 that this texture spin represents only a small part of the total texture change. This is corroborated by Fig. 2.21. In this figure the deviation of the texture from its original orthotropic

**Fig. 2.20** Individual lattice rotation  $\Delta g$  (lattice spin) *a* and the average rotation  $\bar{\Delta g}$  (texture spin) *b*

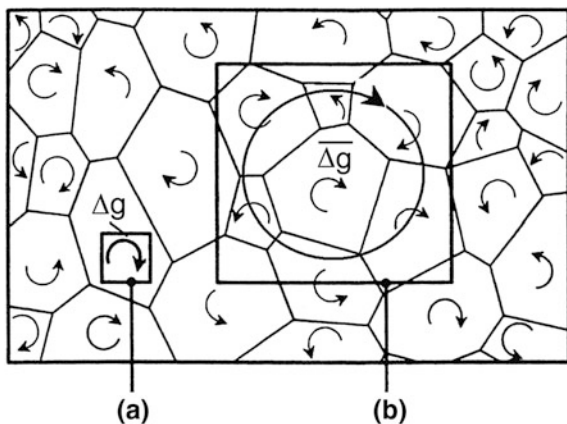
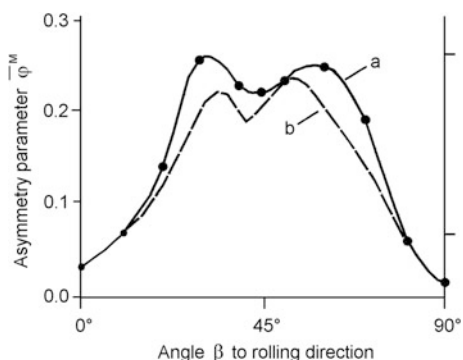


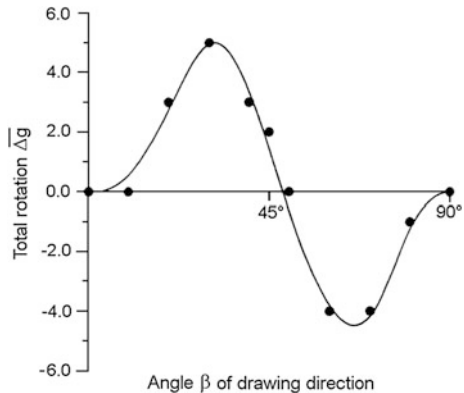
**Fig. 2.21** Deviation of the texture symmetry from the original orthotropic symmetry (as a measure of texture change) for samples cut out of an aluminum sheet and elongated by 20 % under the angle  $\beta$  to the rolling direction: *a* total asymmetry; *b* remaining asymmetry after carrying out the “texture spin” rotation according to Eqs. (2.20) and (2.22)



symmetry (expressed by an asymmetry parameter) is plotted for samples cut out of an aluminum sheet under different angles  $\beta$  to the rolling direction (i.e. to the original orthotropic axes) and elongated by 20 % (Bunge and Nielsen 1997). The upper curve *a* is the total change, the lower curve *b* is obtained after carrying out the texture spin, Eq. (2.22), i.e. the average rotation shown in Fig. 2.20b. The still remaining deviation from orthotropic symmetry, curve *b*, is due to the *individual rotations* shown in Fig. 2.20a. They are much stronger than the “common” rotation component, the texture spin which is shown in Fig. 2.22, as a function of the angle  $\beta$ . It assumes a maximum value of only  $5^\circ$  in this case. Hence, the Cosserat continuum is not an appropriate model to treat plastic deformation to large plastic strains *in terms of polycrystalline volume elements*. In the isotropic Cosserat solid there are six elastic constants, in contrast to the classical elastic solid in which there are two. A polycrystalline volume element requires many more internal parameters, e.g. the texture coefficients  $C_{\lambda}^{\mu\nu}$ , Eq. (2.41).

In order to obtain the *complete texture change* the rotations  $R(g)$  must be considered individually for all orientations  $g$  together with the orientation densities  $f(g)$

**Fig. 2.22** The texture spin  $\Delta g$  according to Eqs. (2.20) and (2.22) and Fig. 2.20 for samples cut out of an aluminum sheet and elongated 20 % under the angle  $\beta$  to the rolling direction



in these orientations. Hence, the texture change during a *small deformation step*  $d\eta$  is described by the *continuity equation* in the orientation space  $g$  (Clement and Coulomb 1979):

$$\frac{\partial f(g, \eta)}{\partial \eta} = -\text{div}\{f(g, \eta) \cdot R(g)_\varepsilon\} = \phi(g, \eta)_\varepsilon \quad \text{Continuity Equation.} \quad (2.23)$$

Equation (2.23) expresses the fact that no orientations “get lost” in the orientation space. They rather move continuously into and out of any volume element in this space in which the density  $f(g)$  is defined. In this respect the texture is analogous to a compressible fluid in the orientation space with local density  $f(g)$ . After larger deformation the end-texture  $f^{\text{end}}(g)$  is reached. It is obtained by integration over all small steps  $d\eta$ . Thereby it must be admitted that the deformation tensor  $\varepsilon_{ij}$  (i.e. the deformation geometry) may vary with the deformation degree  $\eta$ . Hence, the *deformation path*  $\varepsilon(\eta)$  must be taken into account, and it is obtained after *large deformations* by

$$f^{\text{end}}(g) = f^{\text{start}}(g) + \int_{\eta^{\text{start}}}^{\eta^{\text{end}}} \phi(g, \eta, \varepsilon(\eta)) d\eta \quad \text{Large Deformations.} \quad (2.24)$$

As a special case, the deformation path  $\varepsilon(\eta)$  may also be constant, as for instance during uniaxial elongation in the homogeneous range.

### 2.5.2 Special Plasticity Parameters

Having Eqs. (2.12a) and (2.12b) in mind, it is meaningful to split the deformation tensor, Eq. (2.10), into its symmetric and antisymmetric part

$$\varepsilon_{ij} = \varepsilon_{ij}^{\text{sym}} + \varepsilon_{ij}^{\text{ant}}. \quad (2.25)$$

The first one is a shape change of the volume element, the second one is a rigid rotation (which is to be distinguished from the lattice rotation  $R_{ij}$  in Eq. (2.12)). The symmetric part can be referred to its *principle axes* which are related to the chosen sample coordinate system  $K_A$  by the rotation  $g_\varepsilon$

$$\varepsilon_{kl}^{\text{sym}} = \begin{bmatrix} 1 & 0 & 0 \\ 0 & -q & 0 \\ 0 & 0 & -(1-q) \end{bmatrix}_{g_\varepsilon} \quad \text{Principle Strain Axes.} \quad (2.26)$$

By the choice of  $d\eta$  the component  $\varepsilon_{11}$  in Eq. (2.26) can always be normalized to one. As is seen in Eqs. (2.12a) and (2.13), the monocrystal Taylor factor  $M$  depends only on the symmetric part of the imposed strain  $\varepsilon^{\text{sym}}$ . With Eq. (2.19) the same holds for the polycrystal Taylor factor  $\bar{M}$ . Hence, we can write

$$\bar{M}(\varepsilon) = \bar{M}(\varepsilon^{\text{sym}}) = \bar{M}(q, g_\varepsilon). \quad (2.27)$$

If we know the principle strain axes a priori then we can choose them as the sample coordinate system  $K_A$ . In this case the polycrystal Taylor factor depends only on one parameter, namely  $q$  (assuming of course that the texture is given and does not change during the small deformation step).

According to Eq. (2.21) the Taylor factor  $\bar{M}$  describes the deformation work needed during the deformation step  $d\eta$ . If the parameters  $q$  and  $g_\varepsilon$  in Eq. (2.27) are not fixed by the deformation device, then they will assume such values which minimize Eq. (2.27):

$$\bar{M}(q, g_\varepsilon) \rightarrow \min. \quad (2.28)$$

The minimum values depend on the texture and hence, they are material property parameters, describing plastic anisotropy.

We consider particularly the following two simple experimental conditions:

### Uniaxial Stress, r-Value

In a uniaxial tensile test a uniaxial *stress* is applied. This enforces a strong *strain* component along the stress direction. Nevertheless, the principle strain axes may deviate from the principle stress axes, Fig. 2.23. In many cases (of not too strong texture) these deviations may, however, be neglected. Then  $g_\varepsilon$  in Eq. (2.28) is fixed and  $\bar{M}$  has to be minimized with respect to  $q$  only:

$$\frac{d\bar{M}(q)}{dq} = 0 \quad \rightarrow \quad q_{\min}. \quad (2.29)$$



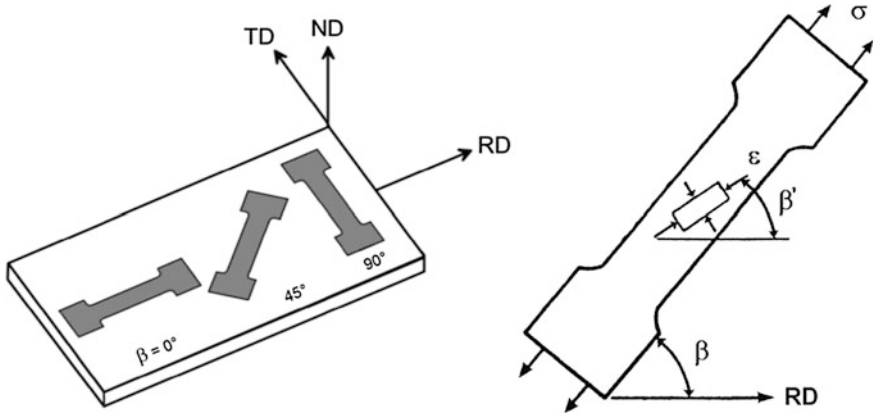


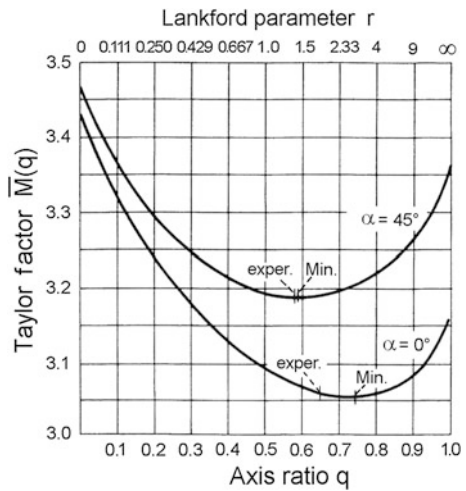
**Fig. 2.23** In a uniaxial tensile test under the angle  $\beta$  towards sheet-rolling direction the principle strain axes  $\varepsilon$  may deviate from the principle stress axes  $\sigma$

The minimum value of  $q$  is related to the *Lankford parameter*  $r$  by

$$r = \frac{q_{\min}}{1 - q_{\min}}. \quad (2.30)$$

This is illustrated in Fig. 2.24 for two samples cut in rolling direction and under  $45^\circ$  from a rolled iron sheet. The curves were calculated from the measured texture by Eq. (2.19) as a function of  $q$ . The experimental  $q$ -value agrees quite well with the calculated minimum value according to Eq. (2.29) (Bunge and Roberts 1969; Bunge 1970).

**Fig. 2.24** The polycrystal Taylor factor  $\bar{M}(q)$  as a function of  $q$  (for a given texture) compared with the experimentally determined  $q$ -value, respectively  $r$ -value according to Eq. (2.30)



### Biaxial Stress, Yield Locus

A biaxial stress may be applied to the material. It can be represented in the *principle stress axes* which have the orientation  $g_\sigma$  with respect to the sample coordinate system  $K_A$ :

$$\sigma_{ij} = \begin{bmatrix} \sigma_1 & 0 & 0 \\ 0 & \sigma_2 & 0 \\ 0 & 0 & 0 \end{bmatrix}_{g_\sigma} \quad \text{Principle Stress Axes.} \quad (2.31)$$

In the most general case the *principle strain axes*  $g_\varepsilon$  in Eq. (2.26) need not be parallel to the principle stress axes of Eq. (2.31) as was illustrated in Fig. 2.23. If, however, the material has orthorhombic (orthotropic) symmetry, as in the case of sheet metals, and if we choose the principle stress axes parallel to the orthotropic axes of the material, i.e. to the symmetry axes of the texture, then they are also the principle strain axes  $g_\varepsilon$  of Eq. (2.26). The deformation work (Eq. (2.21)) can then be expressed by the stress and strain tensor

$$\begin{aligned} d\bar{W} &= d\eta \cdot \varepsilon_{ij} \cdot \sigma_{ij} \\ &= d\eta \cdot [\sigma_1 - q \cdot \sigma_2] = \tau_0 \cdot d\eta \cdot \bar{M}(q). \end{aligned} \quad (2.32)$$

For any given value of  $q$ , Eq. (2.32) represents a straight line in the principle stress-space  $\sigma_1, \sigma_2$  which is a tangent to the yield locus. The yield locus is then obtained as the inner envelope of the bunch of these straight lines. By differentiating Eq. (2.32) with respect to  $q$  one obtains, together with Eq. (2.32), (Bunge et al. 1980; Park et al. 1993)

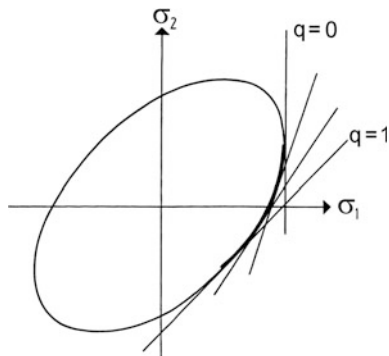
$$\begin{aligned} \sigma_1 &= \left[ \bar{M}(q) - q \cdot \frac{d\bar{M}(q)}{dq} \right] \cdot \tau_0 \\ \sigma_2 &= - \frac{d\bar{M}(q)}{dq} \cdot \tau_0 \end{aligned} \quad (2.33)$$

This is illustrated in Fig. 2.25. The *shape* of the yield locus follows from  $\bar{M}(q)$  and hence from the texture, its *size* is given by the hardness parameter  $\tau_0$ .

### 2.5.3 Plasticity of Cubic Metals

Crystal structure enters plastic behavior, e.g. in the Taylor model, via the glide systems, i.e. via the  $G_{ij}^n$  in Eq. (2.12) expressed by  $\mathbf{d}_i^n$  and  $\mathbf{n}_j^n$  in Eq. (2.11). The glide systems are (in a good first approximation)

**Fig. 2.25** The yield locus is obtained as the inner envelope of a bundle of straight lines as a function of  $q$  (cf. Eq. (2.32))



$$\begin{aligned} \text{for fcc metals : } & \{111\}\langle 110 \rangle \\ \text{for bcc metals : } & \{110\}\langle 111 \rangle \end{aligned} \quad (2.34)$$

i.e. glide plane normal and glide direction are exchanged in the two crystal structures. Then it follows immediately from Eq. (2.11)

$$\begin{aligned} G_{ij}^n(g)_{\text{bcc}}^{\text{sym}} &= G_{ij}^n(g)_{\text{fcc}}^{\text{sym}} \\ G_{ij}^n(g)_{\text{bcc}}^{\text{ant}} &= -G_{ij}^n(g)_{\text{fcc}}^{\text{ant}} \end{aligned} \quad (2.35)$$

and for the two principle quantities of plasticity,  $M$  and  $R$ :

$$\begin{aligned} M(g)_{\text{bcc}} &= M(g)_{\text{fcc}} \\ R_{ij}(g)_{\text{bcc}} &= -R_{ij}(g)_{\text{fcc}}. \end{aligned} \quad (2.36)$$

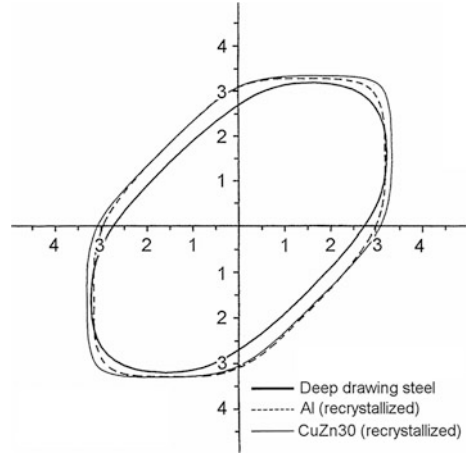
Hence, with the same texture, fcc and bcc metals have the same (polycrystal) Taylor factor

$$\bar{M}_{\text{bcc}} = \bar{M}_{\text{fcc}} \quad \text{Same Texture } f(g) \quad (2.37)$$

and therefore the same plastic anisotropy expressed, for instance, by the  $r$ -value, Eq. (2.30), or by the yield locus, Eq. (2.33).

As an example Fig. 2.26 shows the yield loci of three different fcc and bcc materials calculated from their respective textures. All three yield loci are in between those according to the von Mises and Tresca hypotheses. The differences are due to the different rolling textures. Because of Eq. (2.37), fcc and bcc materials *with the same given texture* need not be distinguished in plasticity model calculations *for small deformations*. Because of Eq. (2.36b), however, the orientation changes of fcc and bcc crystals by plastic deformation go into opposite directions. Hence, with the *same starting texture different end-textures* will result after the

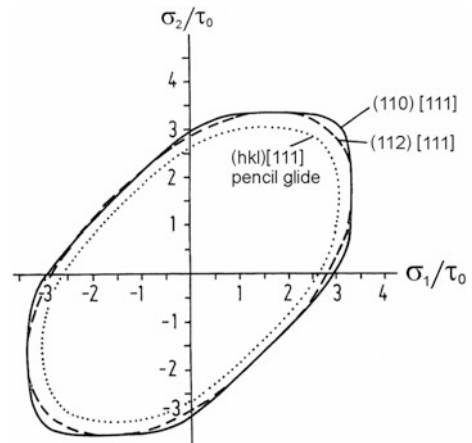
**Fig. 2.26** Yield loci of various materials calculated from their textures



same (large) plastic deformation according to Eq. (2.24). Therefore, plastic behavior of these two kinds of materials is different *after large deformation*.

Finally Fig. 2.27 illustrates the influence of different glide systems on the yield locus with the same texture (in this case random crystal orientation distribution is assumed). Glide systems  $\{111\}\langle 112 \rangle$  have been considered (at least in addition to  $\{111\}\langle 110 \rangle$ ) for fcc metals with low stacking fault energy such as brass and silver. Pencil glide  $\{hkl\}\langle 111 \rangle$  is assumed to be the best-fitting deformation mode for bcc metals. Taking different glide systems into account then Eq. (2.36) is no more strictly valid, but it is still a good first approximation.

**Fig. 2.27** Yield loci calculated for three different glide systems



### 2.5.4 Deformation Hardening

Any change of the flow stresses  $\sigma$  in the course of deformation is generally called *deformation hardening*. The stresses are obtained by minimizing the deformation work, Eq. (2.21), from which particularly Eq. (2.33) was obtained in that special case.

Hence, total hardening can be split into the following three contributions due to changes of the three parameters  $\tau_0$ ,  $a^n$  and  $f(g)$  entering this expression

$$\left(\frac{\partial\sigma}{\partial\eta}\right)_{a^n, f(g)} = \frac{\partial\sigma}{\partial\tau_0} \cdot \frac{d\tau_0}{d\eta} \quad \text{Isotropic Strain Hardening} \quad (2.38)$$

$$\left(\frac{\partial\sigma}{\partial\eta}\right)_{\tau_0, f(g)} = \frac{\partial\sigma}{\partial a^n} \cdot \frac{da^n}{d\eta} \quad \begin{array}{l} \text{Anisotropic Strain Hardening} \\ \text{"Latent Hardening"} \end{array} \quad (2.39)$$

$$\left(\frac{\partial\sigma}{\partial\eta}\right)_{\tau_0, a^n} = \frac{\partial\sigma}{\partial f(g)} \cdot \frac{df(g)}{d\eta} \quad \text{Texture Hardening.} \quad (2.40)$$

It is worth mentioning that all three parts may assume also negative values (softening). This is particularly known as the *Bauschinger Effect* and as *deformation softening* (negative strain hardening) as well as *texture softening*. The prevailing case is, however, positive hardening.

Anisotropic strain hardening (latent hardening) is often assumed to be small compared with isotropic strain hardening. In this case strain hardening is a multiplicative factor  $\tau_0$ , Eqs. (2.21) and (2.33). This factor does not enter Eqs. (2.29) and (2.30). Hence, the  $r$ -value is a plasticity parameter which is independent of the actual hardening state of the material (which may be different when different samples are being compared). Texture hardening (or softening) can be deduced from the texture change according to Eq. (2.23) for small deformation steps (where it is generally small compared to strain hardening), and from Eq. (2.24) for large strains in which case it must not be neglected.

### 2.5.5 Plasticity of Macroscopic Bodies

On the *mesoscopic* scale we have considered a polycrystalline volume element  $V_{\mathbf{X}}$  (type d in Fig. 2.15) which is characterized by its texture  $f(g)$  and its hardness described by  $\tau_0^n$ . Both quantities may vary as a consequence of deformation.

On the *macroscopic* scale (process-relevant scale) many such polycrystalline volume elements at the loci  $\mathbf{X}$  must be considered. They undergo the local deformation  $\bar{\epsilon}(\mathbf{X})$  (deformation field) which may even vary in the course of deformation as a function of  $\eta$  (deformation path). Hence, each volume element may develop its own texture (texture field  $f(g, \mathbf{X})$ ) as well as its own hardness  $\tau_0^n(\mathbf{X})$ , both as a

function of the actual deformation degree  $\eta$ . The deformation field  $\bar{\epsilon}(\mathbf{X})$  is not uniquely fixed by the external conditions. Rather, stresses and/or strains are given only on the surface of the body. The stress and strain *fields*  $\bar{\epsilon}(\mathbf{X})$  and  $\sigma(\mathbf{X})$  develop according to minimum *total* deformation energy which involves the actual materials *property fields*  $f(g, \mathbf{X}, \eta)$  and  $\tau_0^a(\mathbf{X}, \eta)$ . Hence, any plasticity model of macroscopic bodies must consider local textures and local hardness simultaneously (see e.g. (Hoferlin et al. 1999)).

## 2.6 Parameterization of the Texture Function

The texture function  $f(g)$ , defined in Eq. (2.2), is the basic quantity for the calculation of the plastic properties of a polycrystalline material from the known properties of monocrystals expressed in Eq. (2.19). The function  $f(g)$  is a function of three variables. It requires several thousand function values for its numerical representation and treatment (depending on the required angular resolution and hence accuracy). This number can be drastically reduced by choosing an appropriate *parameterization* of this function. For this purpose we express  $f(g)$  by a series expansion in terms of generalized spherical harmonics  $T_\lambda^{\mu\nu}(g)$  (Bunge 1982):

$$f(g) = \sum_{\lambda=0}^L \sum_{\mu=1}^{M(\lambda)} \sum_{\nu=1}^{N(\lambda)} C_\lambda^{\mu\nu} \cdot T_\lambda^{\mu\nu}(g). \quad (2.41)$$

The “resolving power” of this representation is given by the series truncation value  $L$ . The function  $f(g)$  is then represented by its coefficients  $C_\lambda^{\mu\nu}$ , the number of which depends on  $L$ . The coefficients are obtained from experimental measurements of pole figures by a mathematical procedure called *Pole Figure Inversion* for which routine computer programs have been developed (Dahms and Bunge 1989; Dahlem-Klein et al. 1993; Schäfer 1998). The positivity of ODF and pole figures, as statistical density functions, is taken into account during the iterative calculation so that “ghost” errors are eliminated. The result of this procedure was illustrated in Fig. 2.5.

In order to calculate the basic integral Eq. (2.19), the function  $M(g)$  is represented in the same way (Bunge 1970) as well:

$$M(g) = \sum_{\lambda=0}^{L_0} \sum_{\mu=1}^{M(\lambda)} \sum_{\nu=1}^{N(\lambda)} m_\lambda^{\mu\nu} \cdot T_\lambda^{\mu\nu}(g). \quad (2.42)$$

Thereby the truncation value  $L_0$  may be chosen different from  $L$  in Eq. (2.41). The coefficients  $m_\lambda^{\mu\nu}$  can be obtained from  $M(g)$  by a known mathematical procedure, see e.g. (Bunge 1982). The integral Eq. (2.19) then takes on the form

$$\bar{M} = \sum_{\lambda=0}^{L_{\min}} \sum_{\mu=1}^{M(\lambda)} \sum_{\nu=1}^{N(\lambda)} \frac{C_{\lambda}^{\mu\nu} \cdot m_{\lambda}^{\mu\nu}}{2\lambda + 1}; \quad L_{\min} = \min[L, L_0]. \quad (2.43)$$

It turns out that usually the series Eq. (2.42) converges much faster than that of Eq. (2.41), i.e.  $L_0 < L$ . In fact, rather low values of  $L_{\min}$  are often satisfactory. Hence, Eq. (2.43) provides a very “economic” mathematical treatment of the “Texture  $\rightarrow$  Property” relationship illustrated on the right side of Fig. 2.9 (here applied to plastic properties).

In cubic materials the lowest-order non-random approximation is  $L_{\min} = 4$ . With this approximation the  $r$ -value in sheet metals, according to Eqs. (2.29) and (2.30), in the sheet plane, Fig. 2.11, can be written in the form

$$r(\beta) = 1 + r_1 C_4^{11} + r_2 C_4^{12} \sin 2\beta + r_3 C_4^{13} \sin 4\beta. \quad (2.44)$$

It contains only three texture coefficients  $C_4^{1\nu}$ . Since a similar fourth-order expression describes the elastic properties in sheet materials, too, this may be used as the basis for an (indirect) determination of plastic properties from the more convenient measurement of elastic properties, as was done, for the first time, by Stickels and Mould (Stickels and Mould 1970) and was found satisfactory in many applications.

It must be mentioned, however, that the “Process  $\rightarrow$  Texture” relationship does not allow a satisfactory low-order approximation. This relationship, expressed in Eqs. (2.23) and (2.24), requires the full series expansion Eq. (2.41) with the value  $L$  guaranteeing good convergence of the series (which is the higher the sharper the texture is). As a rule  $L \sim 30$  may be satisfactory in many cases, corresponding to some hundred coefficients  $C_{\lambda}^{\mu\nu}$ . This is much more than the four coefficients of the approximation, but Eq. (2.44) is still one order of magnitude lower than the representation of the texture function  $f(g)$  by several thousand function values. Hence, the parameterization of this function by Eq. (2.41) is “most economic” also for the “Process  $\rightarrow$  Texture” relationship. For details see e.g. (Klein and Bunge 1991).

## 2.7 Other Modes of Plasticity

In the preceding sections we have considered plastic deformation on the basis of dislocation glide (which was averaged to homogeneous shear in the glide systems). In the most general case, however, many other physical processes may also contribute to plastic deformation of materials:

- *Mechanical twinning* leads to homogeneous shear in the twin lamellae, similar to Eq. (2.11). Crystal orientation in these lamellae is, however, changed discontinuously with respect to the starting crystal orientation. Furthermore, the shear stresses  $\tau_0^n$ , by which twinning is “triggered”, are quite different in



twinning and “anti-twinning” direction. Twinning is the main reason for non-centrosymmetric yield loci in the *hexagonal materials*. This is not treated in the present chapter.

- *Grain boundary sliding* leads to highly localized shear strains in the grain boundaries, based on diffusion processes. In this case texture formation contains a strong contribution of rigid rotation of grains with respect to each other. It is assumed that this effect plays an important role in *superplastic deformation* which is also not considered in this chapter.
- *Hot deformation* is characterized by recrystallization processes occurring simultaneously with dislocation glide and hardening. Hence, the texture, and as a result of that plastic anisotropy, are changing in a different way compared to that considered in this chapter. It may be mentioned that the deformation of *low-melting-point materials*, such as lead, may be “hot-deformation” in this sense even at room temperature.
- *Martensitic phase transformation* may be induced by plastic deformation (deformation martensite). This process bears strong analogy to mechanical twinning mentioned above. This process plays a role, for instance, in some steels. It is also the basic process for *shape memory materials*, the deformation of which is also not considered in this chapter.
- *Green-forming* of (moist) ceramic masses is based on sliding and rotation of rigid particles and follows completely different mechanisms as those considered here.
- Finally, the present considerations deal only with crystalline materials as shown in Fig. 2.1 and described in the Microstructure Function, Eq. (2.1). This does not include materials with *amorphous structures* (either completely or partly amorphous) such as polymers or glasses. Plasticity of these materials is thus also not included in this chapter.

Mathematical models for the Process  $\rightarrow$  Texture, Texture  $\rightarrow$  Property relationships (Fig. 2.9) and hence, the plasticity of materials, based on the mentioned mechanisms, are much more complicated than the case treated here, i.e. plasticity based only on dislocation glide. Nevertheless, plasticity based on dislocation glide only is still the most prominent case applicable to the formability of many technologically important materials.

## References

- Bishop JFW, Hill R (1951) A theoretical derivation of the plastic properties of a polycrystalline face-centered metal. *Phil Mag Ser 7*:1298–1307
- Brokmeier HG, Lenser S, Schwarzer R, Ventzke V, Riekehr S, Kocak M, Homeyer J (2007) Crystallographic texture of dissimilar laser welded Al5083-Al6013 sheets. *Mat Sci Forum* 539–543:3894–3899
- Bunge HJ (1970) Some applications of the Taylor theory of polycrystal plasticity. *Kristall Tech* 5:145–175

- Bunge HJ (1982) Texture analysis in materials science—mathematical methods. Butterworths, London. [http://www.ebsd.info/pdf/Bunge\\_TextureAnalysis.pdf](http://www.ebsd.info/pdf/Bunge_TextureAnalysis.pdf)
- Bunge HJ, Klein H (1993) Model calculations of texture changes by non-unique orientation flow fields. In: Lee WB (ed) *Advances in engineering plasticity and its applications*. Elsevier, Amsterdam, pp 109–117
- Bunge HJ, Nielsen I (1997) Experimental determination of plastic spin in polycrystalline material. *Int J Plast* 13:435–446
- Bunge HJ, Roberts WT (1969) Orientation distribution, elastic and plastic anisotropy in stabilized steel sheet. *J Appl Cryst* 2:116–128
- Bunge HJ, Schwarzer RA (2001) Orientation stereology—a new branch in texture research. *Adv Eng Mat* 3:25–39
- Bunge HJ, Schulze M, Grzesik D (1980) Calculation of the yield locus of polycrystalline materials according to the Taylor theory. *Peine+Salzgitter Berichte, Sonderheft*
- Canova GR, Kocks UF, Jonas JJ (1984) Theory of torsion texture development. *Acta Met* 32:211–266
- Chin GY (1969) Tension and compression textures. In: Grewen J, Wassermann G (eds) *Textures in research and practice*. Springer, Berlin, pp 51–80
- Clement A, Coulomb P (1979) Eulerian simulation of deformation textures. *Scr Met* 13:899–901
- Cosserat E, Cosserat F (1909) *Theory of deformable bodies* (in French). A. Hermann et Fils, Paris
- Dahlem-Klein E, Klein H, Park NJ (1993) Program system ODF analysis. Cuvillier Verlag, Göttingen
- Dahms M, Bunge HJ (1989) The iterative series-expansion method for quantitative texture analysis: I. General outline. *J Appl Cryst* 22:439–447
- Dawson PR, Beaudoin AJ (1998) Finite element simulation of metal forming. In: Kocks UF, Tomé CN, Wenk HR (eds) *Texture and anisotropy*. Cambridge University Press, pp 532–558
- Dawson PR, Beaudoin AJ, Mathur KK (1994) Finite element modelling of polycrystalline solids. *Mat Sci Forum* 157–162:1703–1712
- Fischer AH, Schwarzer RA (1998) Mapping of local residual strain with an X-ray scanning apparatus. *Mat Sci Forum* 273–275:673–677
- Hoferlin E, van Bael A, van Houtte P (1999) Influence of texture evolution on finite element simulation of forming processes. In: Szpunar J (ed) *Proceedings of 12th international conference on textures of materials (ICOTOM-12)*. NRC Research Press, Ottawa, pp 249–254
- Honneff H, Mecking H (1978) A method for the determination of the active slip systems and orientation changes during single crystal deformation. In: Gottstein G, Lücke K (eds) *Proceedings of 5th international conference on texture of materials (ICOTOM-5)*, vol 1. Springer, Berlin, pp 265–275
- Iwakuma T, Nemat-Nasser S (1984) Finite element elastic-plastic deformation of polycrystalline metals. *Proc Roy Soc London A* 394:87–119
- Klein H, Bunge HJ (1991) Modelling deformation texture formation by orientation flow-field. *Steel Res* 62:548–559
- Kocks UF, Tomé CN, Wenk HR (1998) *Texture and anisotropy*. Cambridge University Press
- Kröner E (1961) On the plastic deformation of the polycrystal (in German). *Acta Met* 9:155–161
- Leffers T (1988) Deformation textures: simulation principles. Panelist's contribution. In: Kallend JS, Gottstein G (eds) *Proceedings of 8th international conference on textures of materials (ICOTOM-8)*. The Metallurgical Society of AIME, Warrendale, pp 273–284
- Leffers T, Asaro RJ, Driver JH, Kocks UF, Mecking H, Tomé C, Van Houtte P (1988) Deformation textures: simulation principles. Panel report, pp. 265–272
- Lippmann H (1969) A Cosserat theory of plastic flow (in German). *Acta Met* 8:255–284
- Lippmann H (1995) Cosserat plasticity and plastic spin. *Appl Mech Rev* 48:753–762
- Lowe TC, Rollett AD, Follansbee PS, Daehn GS (1991) Modelling the deformation of crystalline solids: physical theory, applications, and experimental comparison. The Metallurgical Society of AIME, Warrendale
- Masson R, Zaoui A (1999) Self-consistent estimates for the rate-dependent elastoplastic behaviour of polycrystalline materials. *J Mech Phys Solids* 47:1543

- Molinari A, Canova GR, Ahzi S (1987) A self-consistent approach of the large deformation polycrystal viscoplasticity. *Acta Met* 35:2983–2994
- Park NJ, Klein H, Dahlem-Klein E (1993) Program system physical properties of textured materials. Cuvillier Verlag, Göttingen
- Raabe D (1998) Computational materials science. Wiley-VCH, Weinheim
- Sachs G (1928) On the derivation of a yield condition (in German). *Z Ver Dtsch Ing (Z VDI)* 72:734–736
- Schäfer B (1998) ODF computer program for high-resolution texture analysis of low-symmetry materials. *Mat Sci Forum* 273–275:113–118
- Schumann H (1979) Crystal geometry—introduction to the theory of lattice transformations of metallic materials (in German). VEB Deutscher Verlag für Grundstoffindustrie, Leipzig
- Schwartz AJ, Kumar M, Adams BL, Field DP (eds) (2009) Electron backscatter diffraction in materials science. Springer Science+Business Media, New York
- Schwarzer RA (1997) Automated crystal lattice orientation mapping using a computer controlled SEM. *Micron* 28:249–265
- Schwarzer RA (2005) Texture mapping by scanning X-ray diffraction and related methods. In: Singh AK (ed) *Advanced X-ray techniques in research and industry*. IOS Press, Amsterdam, pp 50–65
- Spieß L, Teichert G, Schwarzer R, Behnken H, Genzel C (2016) *Modern X-Ray diffraction (in German)*, 3rd edn. Springer Fachmedien GmbH, Wiesbaden
- Stickels CA, Mould RR (1970) The use of Young's modulus for predicting the plastic strain ratio of low carbon steels. *Met Trans* 1:1303–1312
- Taylor GI (1938) Plastic strain in metals. *J Inst Metals* 62:307–324
- Tomé CN, Canova GR (1998) Self-consistent modelling of heterogeneous plasticity. In: Kocks UF, Tomé CN, Wenk R (eds) *Texture and anisotropy*. Cambridge University Press
- Tóth LS, Molinari A, Raabe D (1997) Modelling of rolling texture development in a ferritic chromium steel. *Met Trans A* 28:2343–2351
- Van Houtte P (1984) Some recent developments in the theories for deformation texture prediction. In: Brakman CM, Jongenburger P, Mittemeijer EJ (eds) *Proceedings of 7th international conference on textures of materials (ICOTOM-7)*. Netherlands Society for Materials Science, Zwijndrecht, pp 7–13
- Van Houtte P (1996) Microscopic strain heterogeneity and deformation texture prediction. In: Liang Z, Zuo L, Chu Y (eds) *Proceedings of 11th international conference on textures of materials (ICOTOM-11)*. International Academic Publishers, Beijing, pp 236–247
- Wassermann G, Grewen J (1962) *Textures of metallic materials (in German)*. Springer, Berlin
- Wilson DV (1966) Plastic anisotropy in sheet metals. *J Inst Metals* 94:84–93
- Zaoui A (1986) Quasi-physical modelling of plastic behaviour of polycrystals. In: Gittus J, Zarka J (eds) *Modelling small deformations of polycrystals*. Elsevier, Amsterdam, pp 187–225

Multiscale Modelling in Sheet Metal Forming

Banabic, D. (Ed.)

2016, XIII, 405 p. 137 illus., Hardcover

ISBN: 978-3-319-44068-2